PCCP

Accepted Manuscript

Volume 1 | Number 1 | Jan 2013 | Pages 1–100

PCCP

Physical Chemistry Chemical Physics

www.rsc.org/pccp

ROYAL SOCIETY
OF CHEMISTRY

www.rsc.org/pccp

Electronic properties of $PbX_3CH_3NH_3$ (X=Cl, Br, I) compounds for photovoltaic and photocatalytic applications

Sigismund Teunis Alexander George Melissen[1], Frédéric Labat[2], Philippe Sautet[1], Tangui Le Bahers[1]*

[1] Université de Lyon, Université Claude Bernard Lyon1, Centre National de Recherche Scientifique, ENS Lyon, 46 allée d'Italie, 69007 Lyon Cedex 07, France
[2] PSL Research University, Institut de Recherche de Chimie Paris, CNRS–Chimie ParisTech, 11 rue Pierre et Marie Curie, 75005 Paris, France.

Abstract

Since the discovery of their excellent performance as the light-absorbing semiconducting component in photovoltaic cells, the $PbX_3CH_3NH_3$ (X=I,Br,Cl) perovskites have received renewed attention. The five polymorphs stable above 200K - the tetragonal phases for X=I,Br,Cl and the cubic phases for X=I,Br - were studied using periodic DFT calculations involving hybrid functionals (PBE0 and HSE), employing Gaussian-Type Orbitals as well as plane waves and including relativisitic effects (spin-orbit coupling). The influence of the halogen substitution and of the crystal phase on these properties are analysed by comparing the properties obtained in this study to the experimental ones and to the theoretical ones computed using other methods. We show that an accurate treatment of these systems requires the description of dispersion forces and spin orbit coupling. The different time scales for the electronic and vibrational components of the polarizability inspire the hypothesis that several interfacial charge transfer mechanisms are encountered in the working principle of the photovoltaic devices involving these perovskite materials. The heavy elements in the structure (Pb, I) play a major role in the high polarizability and the low effective charge carrier masses and hence for the low exciton binding energies and the high charge mobility. This systematic work on the $PbX_3CH_3NH_3$ family offers to theoreticians an overview of the landscape of quantum chemical methods to enable a reasonable choice of methodology for studying these systems.

Keywords list: $PbX_3CH_3NH_3$, DFT, HSE, dielectric constant, exciton, photovoltaics

***Corresponding author:** Tangui Le Bahers, tangui.le_bahers@ens-lyon.fr

TOC:

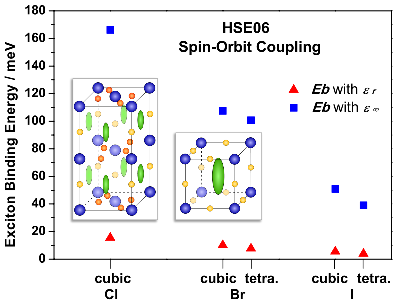

Applying DFT (HSE + spin orbit coupling) computed properties to five perovskites in the PbX$_3$CH$_3$NH$_3$ (X=I,Br,Cl) family of photovoltaic materials reveals that they can exhibit several interfacial charge transfer mechanisms.

I. Introduction

In 2009, Kojima *et al.* were the first to propose a solar cell inspired by the Dye-Sensitized Solar Cell architecture[1] where the dye was replaced by a light-absorbing layer composed of the $PbI_3CH_3NH_3$ semiconductor having a perovskite structure.[2] In this seminal work the authors used the standard liquid electrolyte of Grätzel cells containing the redox couple (I_3^-/I^-) as hole transporting medium. The technology was improved with the replacement of this liquid electrolyte by a hole conducting material, 2,2',7,7'-tetrakis(N,N'-di-*p*-methoxyphenylenamine)-9,9'-spirobifluorene (spiro-OMeTAD), giving rise to a fully solid solar cell and achieving photoconversion efficiencies above 10%.[3] Due to the invested efforts to further develop this technology,[3–7] the photoconversion efficiency achieved today is almost 18%,[8] meaning that 15% of efficiency was gained during five years of development, amounting to an unprecedented growth among the different existing photovoltaic technologies.

In these perovskite cells, light is harvested by a compound of the perovskite family sandwiched between a large bandgap semiconductor (such as TiO_2 or Al_2O_3) and a hole transporting material (spiro-OMeTAD). The photogenerated hole is transferred to the hole transporting material and then to a counter electrode usually containing gold, while the electron can be transferred to a n-type oxide (in the case of TiO_2) or transported by the perovskite itself toward a thin conductive oxide in the case of Al_2O_3 (See Figure 1).

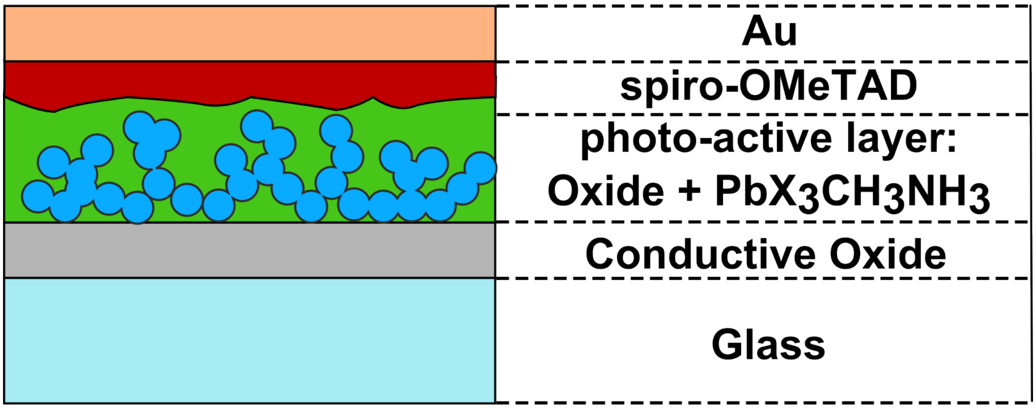

Figure 1. Architecture of a solar cell containing the perovskite compound.

The semiconductor family with the best efficiencies has the chemical formula $PbX_3CH_3NH_3$ (with X=Cl, Br, I) and their mixtures. They were first synthesized during the 1970's[9] and met a renewal of interest during the 1990's,[10–14] because of the nonlinear optical phenomena that could result from the assumed large exciton binding energies. The structure resolutions performed on these materials during the last decades have shown that these compounds exhibit a temperature dependent polymorphism, as depicted in Table 1. It must be noted that there is an on going discussion in the literature[15,16] about the exact nature of the space group of the orthorombic phases, i.e., that these phases could be better classified in the *Pnma* space group, which could have consequences for properties of these compounds such as their ferroelectric behavior.

	Crystal System	Space Group	Temperature / K
$PbCl_3CH_3NH_3$	Cubic	$Pm\bar{3}m$	> 179
	Tetragonal	$P4/mmm$	173 – 179
	Orthorhombic[b]	$P222_1$	< 173
$PbBr_3CH_3NH_3$	Cubic	$Pm\bar{3}m$	> 237
	Tetragonal	$I4/mcm$	155 – 237
	Tetragonal	$P4/mmm$	150 – 155
	Orthorhombic[b]	$Pna2_1$	< 144
$PbI_3CH_3NH_3$	Cubic	$Pm\bar{3}m$	> 327
	Tetragonal	$I4/mcm$	162 – 327
	Orthorhombic[b]	$Pna2_1$	< 162

Table 1: Crystal structures of the $PbX_3CH_3NH_3$ (X=Cl, Br, I) family taken from Poglitsch *et al.*[17] [b] See these references and the text for possible corrections to these phases.[15,16] The temperature-dependent polymorphs of compounds highlighted in grey are the ones studied in this work.

Recently, some of us pointed out some fundamental properties that govern the ability of a semiconductor - such as the perovskite compounds presented above - to generate a photocurrent.[18] These properties are the bandgap, $\boldsymbol{E_g}$, governing the absorption of light, the dielectric constant, $\boldsymbol{\varepsilon_r}$, that influences the exciton binding energy and the effective mass, $\boldsymbol{m^*}$, involved in the charge carriers' mobilities μ. Required ranges of values for these quantities are presented in Table 2. A detailed explanation of how these requirements were derived is available in ref 18.

Solar spectrum absorption	Exciton dissociation	Charge carrier diffusion
$1.1\ \text{eV} < \boldsymbol{E_g} < 1.4\ \text{eV}$	$\boldsymbol{E_b} < 25\ \text{meV}$	$\boldsymbol{\mu} > 10\ \text{cm}^2.\text{V}^{-1}.\text{s}^{-1}$
	$\boldsymbol{\varepsilon_r} > 10$	$\boldsymbol{m^*} < 0.5\ \text{m}_e$

Table 2: Requirements on the semiconductors properties for photovoltaic application.

The aim of this article is to review and discuss the intrinsic properties of this family of compounds and to analyze these properties within the framework developed in ref 18 that decomposes the photovoltaic process in three fundamental steps: (1) light absorption, (2) exciton dissociation and (3) charge carrier diffusion. Experimental and theoretical data obtained from the literature are compared to our computational results. From the computational point of view, multiple theoretical studies using different types of calculations on the various representatives of this family have been performed. To create a homogeneous set of computational data, we performed the calculation of all selected properties using the theoretical protocol proposed in ref 18, presented in the computational details along with the specific computational requirements for this particular family of compounds .

Not all crystal structures presented above are relevant for photovoltaic and photocatalytic applications. Indeed, only the ones observed for temperatures above 200 K are considered interesting for practical applications. For this reason, the focus here will be on the tetragonal and cubic phases of $PbBr_3CH_3NH_3$ and $PbI_3CH_3NH_3$ and only on the cubic phase of $PbCl_3CH_3NH_3$ while other phases will be briefly discussed for completion.

The paper is organized as follows: first, the specific computational details are provided, followed by an account of our results organized by topic, starting with the nature of the obtained geometries followed by a discussion on the bandgap, the dielectric constant and the effective masses of the charge carriers. We finally present our conclusions and perspectives.

II. Computational details.

Geometry optimization and frequency calculations were performed employing the *ab initio* CRYSTAL14 code making use of localized (Gaussian) basis sets,[19,20] using the GGA functionals PBE[21] and PBEsol[22], the global hybrid functionals PBE0[23] and B3PW91[24] and the range separated hybrid functional HSE[30,31] and solving the Hartree-Fock and Kohn-Sham equations self-consistently, thus allowing efficient use of the hybrid functionals. For the C ((10s4p1d)[3s2p1d]), N ((10s4p1d)[3s2p1d]) and H ((4s1p)[2s1p]) atoms the all-electron double zeta 6-31G(d,p) basis set with polarization functions of Pople *et al.*[25] was used while the all-electron triple zeta basis set of Peintinger *et al.*[26] was used for the Cl ((12s8p1d)[5s4p1d]) and Br ((17s13p8d)[6s5p4d]) atoms. For the I and Pb atoms, the small core fully relativistic pseudopotentials developed at Stuttgart University were used along with the double zeta basis set for I (25 valence electrons, (18s13p7d)[4s3p2d]) and the basis set for Pb (22 valence electrons, (18s18p8d1f)[4s4p3d1f]).[27] Reciprocal space was sampled according to a sublattice with a 8×8×8 k-points mesh. To take into account dispersion interactions, the semi-empirical method proposed by S. Grimme, known as +D2, was used.[28] The convergence criterion for the SCF cycle was fixed at 10^{-7} Ha. Geometry optimizations were performed under the constraints that the structures remain cubic or tetragonal depending on the crystal phase and that the Pb and I atoms remain in their Wyckoff positions as imposed by the system's space group (see Table 3). The organic cation was initially centred on the ***1b*** and ***4d*** Wyckoff positions of the cubic and tetragonal cell respectively, but was fully allowed to relax during the geometry optimization.

Space Group	Constrain on the cell	Wyckoff positions
$Pm\bar{3}m$	$\boldsymbol{a} = \boldsymbol{b} = \boldsymbol{c}$ $\boldsymbol{\alpha} = \boldsymbol{\beta} = \boldsymbol{\gamma} = 90°$	Pb: ***1a*** (0, 0, 0) I: ***3d*** (0, 0, ½)
I4/mcm	$\boldsymbol{a} = \boldsymbol{b} \neq \boldsymbol{c}$ $\boldsymbol{\alpha} = \boldsymbol{\beta} = \boldsymbol{\gamma} = 90°$	Pb: ***4c*** (0, 0, 0) I: ***4a*** (0, 0, ¼) I: ***8h*** (***x***, ***x***+½, 0)

Table 3. Constrains imposed during the geometry optimization.

Unconstrained geometry optimizations were performed to allow frequency calculations to obtain ε_{vib}. The calculation of vibrational frequencies was performed within the harmonic approximation to the lattice potential using the same computational parameters as for the geometry optimization. Infrared intensities were obtained through the Berry Phase method.[29]

The effective masses without spin-orbit coupling were computed with the CRYSTAL14 code on the constrained PBE0+D2 geometries, but with the range-separated hybrid HSE functional using the same basis set as for geometry optimization, in coherence with the generalized protocol established earlier.[18]

With the exception of the vibrational component of the static dielectric constant $\boldsymbol{\varepsilon_{vib}}$ and the effective masses computed without spin-orbit coupling as detailed above, all properties are computed from single point calculations performed on the geometries obtained from the constrained optimizations employing the Vienna *Ab Initio* Software Package (VASP, 5.3 version)[32–35].

The bandgaps ($\boldsymbol{E_g}$), electronic dielectric constants ($\boldsymbol{\varepsilon_\infty}$) and the effective masses with spin-orbit coupling were computed using the HSE functional on the constrained PBE0+D2 geometries (obtained with the CRYSTAL09 code) including the spin-orbit coupling within the non-collinear formalism framework[36] to take into account the relativistic effects involved by the lead and halogen atoms. These calculations were performed with the VASP code (5.2 version). 6×6×6 and 4×4×2 k-points meshes were used to compute these properties on the cubic and tetragonal structures respectively so as to stay within reasonable computational payload confines. The particular values were chosen such that the grid precision for the calculation of the Hartree-Fock exchange could be systematically reduced (through the NKRED-flag) by a factor 2. A 400 eV cutoff of the plane wave energies was systematically imposed. The core electrons for each atom were described with the Projector Augmented plane Wave (PAW) approach.

The way to compute all properties (exciton binding energy, electron and hole effective masses…) is presented in ref 18.

III. The crystal structure: Cell parameters

A scheme of the primitive cells of the cubic and the tetragonal cells of $PbX_3CH_3NH_3$ is presented in Figure 2.

The cell parameters computed using different functionals for this work are available in the supporting information section. Only the most relevant results are presented in Table 4 along with experimental and computational values obtained by other groups.

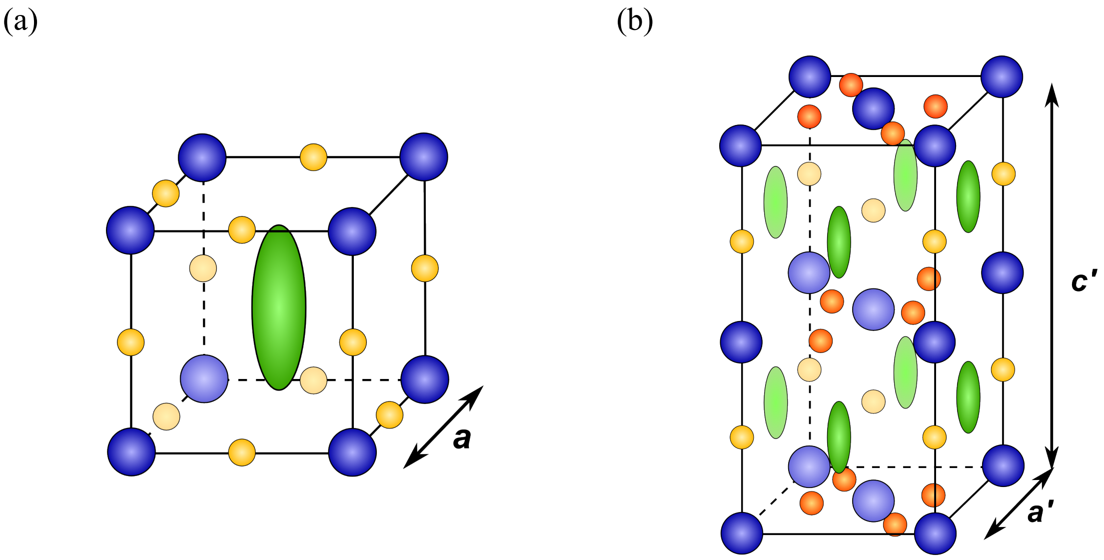

Figure 2. (a) cubic and (b) tetragonal cells of $PbX_3CH_3NH_3$ (X=Cl, Br, I). Blue, yellow, orange and green correspond to the Pb, X (in the *4a* position in the tetragonal cell), X (in the *8h* position in the tetragonal cell) and the organic cation (centred on the *1b* and *4b* positions of the cubic and tetragonal cells respectively).

Using the same functional, PBE, a large range of cell parameters can be computed depending on the basis set type and the basis set size used for plane waves calculations. The cell parameters computed in the references 37–39 using the Quantum Espresso code[40] with a 340 eV (25 Ry) cut-off for basis set size are in better agreement with experiment than the ones computed in ref 41 using the VASP code with a 500 eV cutoff as well as the ones computed in the present study using CRYSTAL14 code with localized basis sets. The cell parameters obtained with VASP and CRYSTAL14 are slightly larger than the experimental ones, which is the expected behaviour for this functional.[42–46] The relatively good agreement obtained in the references 37–39 could be ascribed to the use of a relatively small basis set (a value of 544 eV is recommended for the ultrasoft pseudopotential for Pb atom)[47] giving rise to Pulay stress, artificially compressing the crystal cell during the geometry optimization.[48] The Pulay stress is partly neglected when using a relatively large basis set such as in ref 41 or completely absent when using a localized basis set, such as in the present work. For that reason, the value presented in ref 41 and in this work can be seen as being closer to the PBE limit. This phenomenon was also remarked by Egger *et al*. on PBE based calculations.[49]

The PBEsol functional, which is the revised PBE functional for solids, is in better agreement with the experimental cell parameters than PBE. For semiconductors, the hybrid PBE0 functional is known to give crystal structures in good agreement with experiments.[45,46,44] Nevertheless, in the present case, the cell parameters are overestimated and Grimme's correction is needed to obtain values in better agreement with the experiment, suggesting that dispersion forces are important in these solids. A similar conclusion is obtained by Egger *et al.* who used the Tkatchenko-Scheffler pairwise interaction to simulate the dispersion interaction.[49] These observations are also supported by the studies of Wang *et al.* and Menéndez-Proupin *et al.* performed on the orthorhombic phases of $PbX_3CH_3NH_3$ (X=Cl, Br, I), which show that the use of a functional having a non-local kernel for the correlation - developed to describe Van der Waals interactions - is needed to accurately reproduce cell parameters in comparison with GGA type functionals.[50,51]

To sum up, the inclusion of dispersion forces seems necessary to reproduce the crystalline geometry of these compounds. PBEsol yields lattice parameters smaller than experiment without taking into account Van der Waals interactions, and the nice agreement with experiment may in some cases be due to error cancellation.

method	Basis set type	Basis set size	Ref	$PbCl_3CH_3NH_3$	$PbBr_3CH_3NH_3$			$PbI_3CH_3NH_3$		
				Cubic	Cubic	Tetragonal		Cubic	Tetragonal	
				a	***a***	***a'***	***c'***	***a***	***a'***	***c'***
PBE	PW	340 eV	37						8.76	12.74
PBE	PW	340 eV	38						8.78	12.70
PBE	PW	340 eV	39	5.68	5.90	8.68	12.27	6.33	8.86	12.66
PBE	PW	500 eV	41					6.52		
PBE-TS	PW	700 eV	49	5.71	5.97			6.35	8.89	12.70
PBE	GTO	Dζ + pol[a]		5.72	6.02	8.37	12.12	6.44	8.98	12.85
PBEsol	PW	500 eV	52					6.28		
PBEsol	GTO	Dζ + pol.[a]		5.62	5.90	8.22	11.83	6.29	8.77	12.56
PBE0	GTO	Dζ + pol.[a]		5.70	6.00	8.37	11.99	6.40	8.93	12.79
PBE0+D2	GTO	Dζ + pol.[a]		5.64	5.91	8.23	11.79	6.29	8.76	12.60
Exp			17	5.675	5.901	8.322	11.832	6.325	8.856	12.659

Table 4: Experimental and theoretical cell parameters. Our results are highlighted in grey. PW and GTO stand for Plane-Waves and Gaussian Type Orbitals respectively. "-TS" means Tkatchenko-Scheffler pairwise interaction. [a]"Dζ + pol." means double-zeta basis set + polarization functions (for C, N, H and I atoms). The Pb, Cl and Br atoms were described by a triple-zeta basis set + polarization functions.

IV. The light absorption: Estimation of the bandgap

The bandgap is one of the most important properties for a semiconductor used in a photovoltaic or a photocatalytic device. Shockley and Queisser proved that the maximum photoconversion efficiency achievable by a semiconductor strongly depends on the bandgap and an optimum bandgap range has been defined between 1.1 eV and 1.4 eV for photovoltaic applications.[53,54] In photocatalysis, a different optimum range of bandgap can be defined depending on the specific photocatalytic reaction.

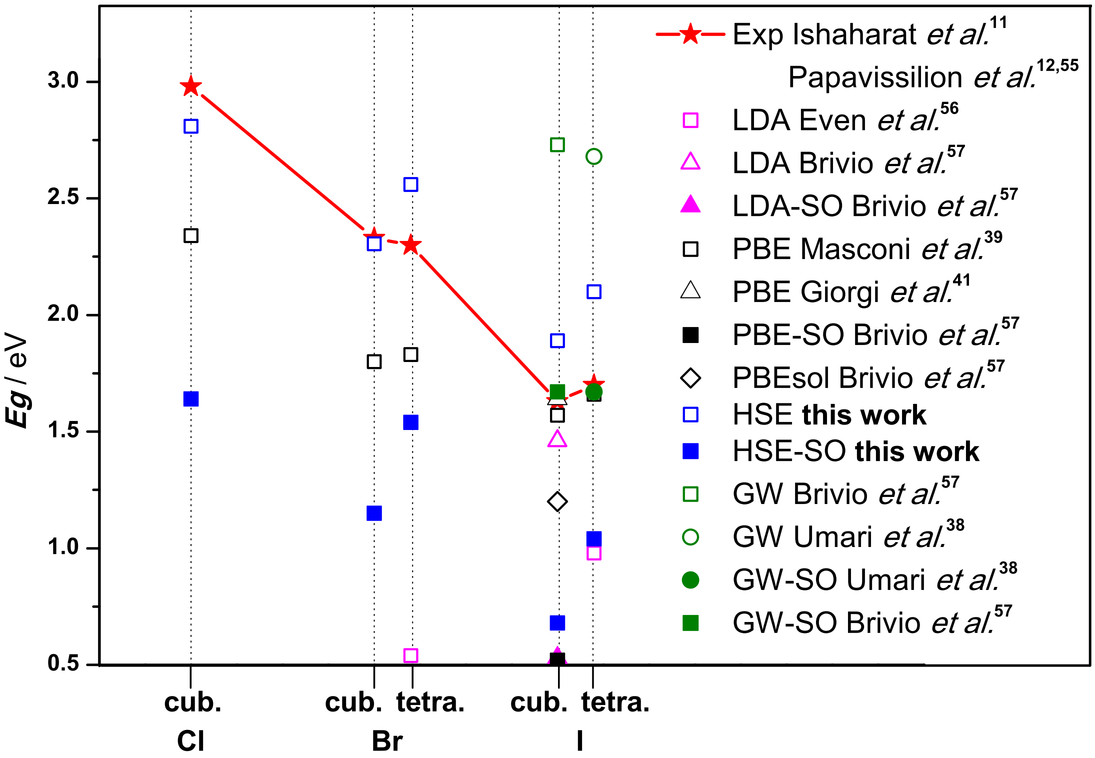

Figure 3. Experimental and theoretical direct bandgaps for $PbX_3CH_3NH_3$ (X=Cl, Br, I). The "-SO" fragment meaning "including spin-orbit coupling".

The experimental bandgaps of the $PbX_3CH_3NH_3$ compounds are presented in Figure 3 along with the computed ones. Experimentally, E_g decreases in the order Cl > Br > I, while the structure (cubic or tetragonal) only has a weak incidence on the bandgap. Only the $PbI_3CH_3NH_3$ material has a bandgap near the optimum for photovoltaic use which explains why this is the most used material in this family for this type of application. Nevertheless, the $PbBr_3CH_3NH_3$ and $PbCl_3CH_3NH_3$ compounds could be interesting for photocatalytic reactions like water splitting, where the bandgap must be around 2 eV, near the bandgap of $PbBr_3CH_3NH_3$.

The calculation of $\boldsymbol{E_g}$ using DFT is clearly not straightforward, as shown by the large statistical dispersion in the values in Figure 3. First, relativistic effects are important, as pointed out by Brivio *et al.*[57] and Umari *et al.*[38] The bandgap reduction caused by spin-orbit coupling as computed with HSE is around 1.1 eV for all systems. Interestingly, the experimentally observed decrease in $\boldsymbol{E_g}$ in the Cl, Br, I series is reproduced with and without including SO-coupling in the calculations. This suggests that the main relativistic effects are associated to the lead atom, rather than the halogens, even for the heavy I atoms. PBE without spin-orbit coupling reproduces quite well the bandgap of these materials, but this is due to error cancellations, since it is known that this functional underestimates the bandgaps of semiconductors.[18,42] PBE artificially reproduces the relativistic effects by underestimating the bandgap. This is confirmed by the calculations performed with PBE by taking into account spin-orbit coupling that gives $\boldsymbol{E_g}$ values that are on average 1.1 eV lower than the experimental ones. Surprisingly, the HSE functional along with the spin-orbit coupling underestimate $\boldsymbol{E_g}$ by 1 eV while this functional is generally known to reproduce bandgaps with an average error of 10%. Interestingly, the influence of the spin-orbit orbit coupling is also to transform the bandgap from to direct to slightly indirect, since for the cubic structure the bottom of the conduction band is slightly offset from the R-point with the spin-orbit coupling while the band gap is direct on the R-point without the spin-orbit coupling. The same phenomenon is computed for tetragonal phases. A description of this spin-orbit coupling induced effect is done by Even *et al*.[58] and in discussed in the section dedicated to the effective masses.

Only post-DFT GW calculations including spin-orbit coupling are able to simulate the bandgap satisfactorily. The failure of standard DFT calculations even with state of the art functionals, and the success of GW, prove that the electron-hole interaction is very strong in these materials and this interaction must be taken into account to reproduce their spectroscopic properties. Probably, the use of the Bethe-Salpeter equations as proposed by Even *et al.*[58] or TD-DFT with an adapted exchange-correlation kernel will improve the spectroscopic description of $PbX_3CH_3NH_3$.[59] The calculated absorption spectra provided by these methods, through the frequency dependant calculation, are richer in information than the value of the bandgap itself.

V. The exciton dissociation

Light absorption generates an exciton, an electron and a hole interacting through the Coulomb interaction, that must be dissociated to extract the charge carriers. The exciton is characterized by its binding energy, $\boldsymbol{E_b}$, itself a function of the dielectric constant of the material and the reduced mass of the exciton ($\overline{m}^*$) with the formula (1) in Wannier's model. This formula shows the role of the dielectric constant in the binding energy demonstrating that particular care must be paid to compute this property.

$$E_b = 13.6\frac{\overline{m}^*}{\varepsilon^2} \qquad (1)$$

where $\boldsymbol{\varepsilon}$ is normally equal to $\boldsymbol{\varepsilon_r}$ but can also considered to be $\boldsymbol{\varepsilon_\infty}$ *(vide infra)*.

1. The dielectric constant.

The dielectric constant is the sum of three terms, the response of the electron density to a change in external electric field, denoted $\boldsymbol{\varepsilon_\infty}$, the vibrational contribution denoted $\boldsymbol{\varepsilon_{vib}}$ and finally the dipole contribution primarily originating from the possible reorientation of dipoles inside the material, $\boldsymbol{\varepsilon_{dip}}$. Only the two first contributions were computed for this work but the last one is the subject of discussion at the end of this section.

$$\varepsilon_r = \varepsilon_\infty + \varepsilon_{vib} + \varepsilon_{dip} \qquad (2)$$

$\boldsymbol{\varepsilon_\infty}$ is linked to the polarizability of the electron density. The larger the polarizability of the electron density, the larger $\boldsymbol{\varepsilon_\infty}$. For this reason, materials containing heavy elements have a high $\boldsymbol{\varepsilon_\infty}$. For the $PbX_3CH_3NH_3$ family, the only values of $\boldsymbol{\varepsilon_\infty}$ available in the literature are 6.5 and 4.8 for the cubic $PbI_3CH_3NH_3$ and $PbBr_3CH_3NH_3$ respectively that are determined from reflectance spectra.[60,10] These values are very close to $\boldsymbol{\varepsilon_\infty}$ of PbI_2 ($\boldsymbol{\varepsilon_\infty} = 6.1$) proving that the organic cation plays only a minor role in that property.[61]

The computed and experimental values of $\boldsymbol{\varepsilon_\infty}$ are presented in Figure 4.

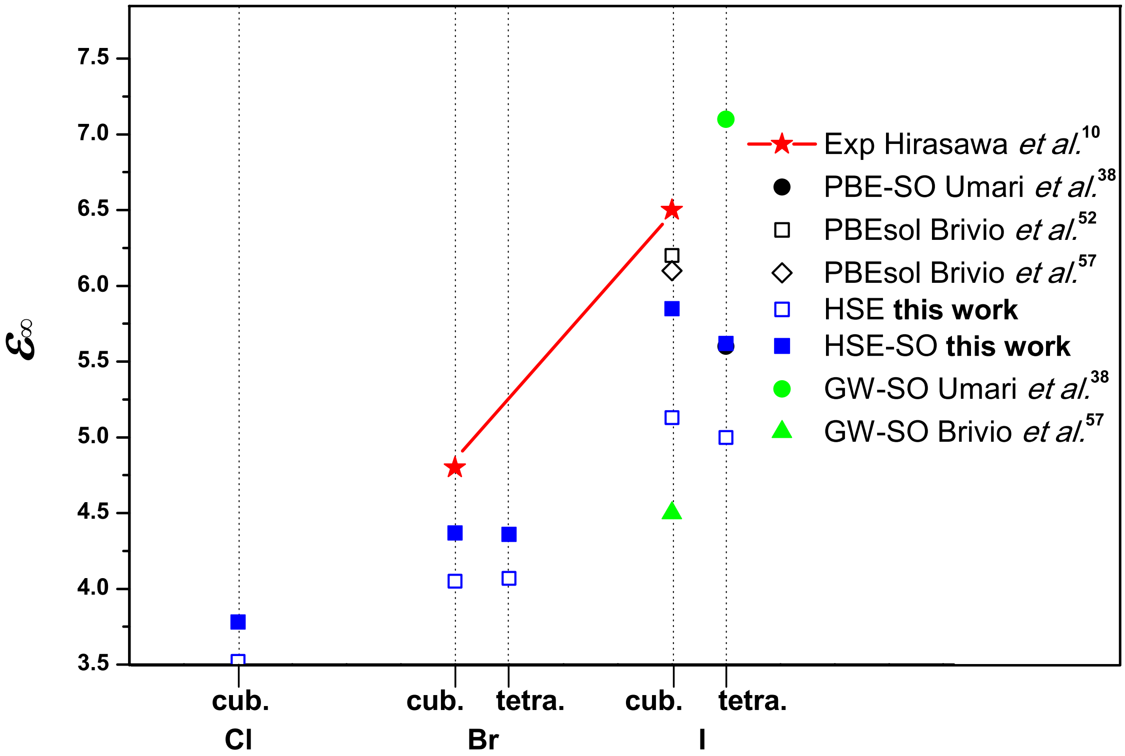

Figure 4. Experimental and Computed values of the electronic contribution to the dielectric constant. The "-SO" label meaning "including spin-orbit coupling".

From a computational point of view, only the dielectric constant of $PbI_3CH_3NH_3$ has been theoretically studied in the literature. As for the bandgap, the calculated values are very sensitive to the method employed. Surprisingly, the best results are not obtained by the GW post-DFT method (even with spin-orbit coupling) but with the GGA functionals PBE and PBEsol. The HSE range separated hybrid is also in nice agreement with the experiment both for $PbI_3CH_3NH_3$ and $PbBr_3CH_3NH_3$, especially if spin-orbit coupling is included. The HSE calculations predict an increase of ε_∞ in the series I > Br > Cl, in agreement with the experiment and coherent with the higher polarizability of the larger halogens. Contrary to the bandgap, the influence of the spin-orbit coupling on ε_∞ increases significantly with the size of the halogen atom. Finally, for $PbCl_3CH_3NH_3$, the value of ε_∞, which is not measured experimentally, is estimated to be around 3.8 with HSE+spin-orbit coupling.

Interestingly, the values of these dielectric constants of $PbX_3CH_3NH_3$ are particularly low compared to other materials used in photovoltaics such as Si (ε_∞ = 12.1) and GaAs (ε_∞ = 10.8). Fortunately, this low value of the electronic contribution is compensated for by a vibrational contribution, ε_{vib}, computed to be around 10 and increasing in the series I > Br > Cl. The simulated IR spectra used to compute ε_{vib} are presented in the supporting information. For each compound, only a few soft vibrational modes (less than 7 per compound) with frequencies below 200 cm^{-1} and involving principally Pb and halogen motions contribute significantly to ε_{vib}.

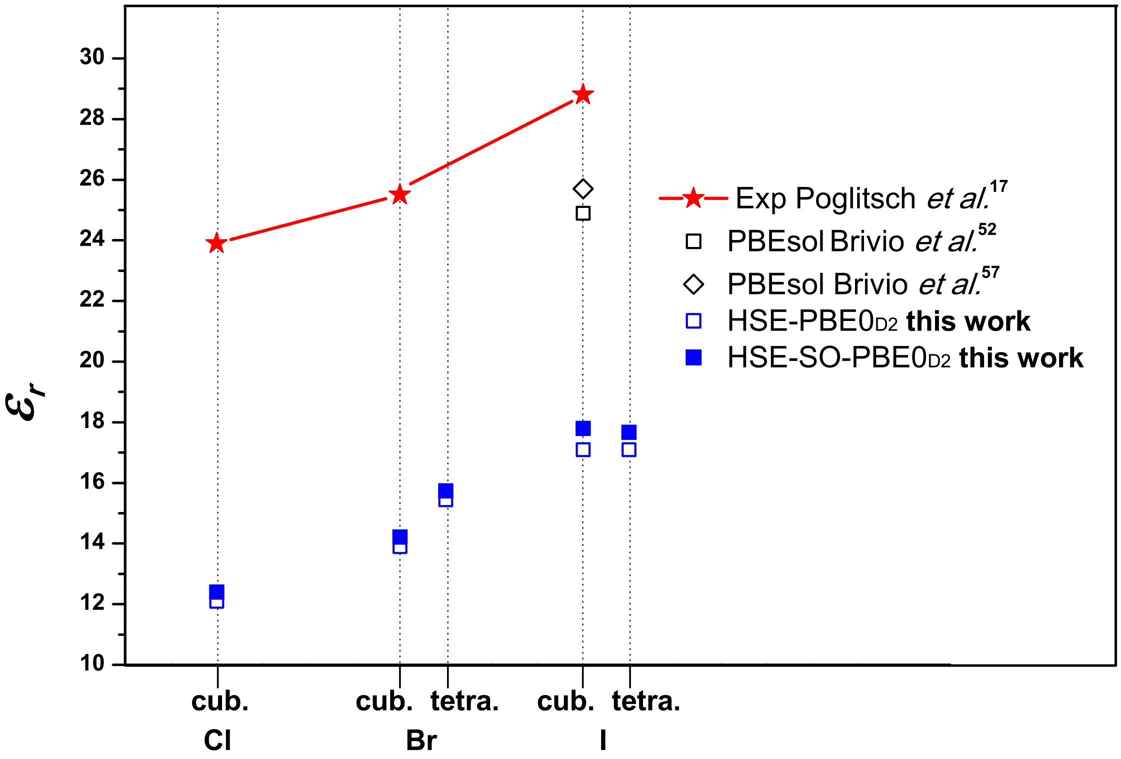

Figure 5. Computed values of the total dielectric constant (including electronic and vibrational contribution). The "-SO" fragment meaning "including spin-orbit coupling".

Interestingly, although not negligible, the vibrational contribution to the dielectric constant is rather low compared to that observed in oxides, suggesting that the Pb-X bond is particularly covalent as also suggested by Lucovsky *et al.* for PbI_2.[61]

In the present work, the vibrational contribution to the dielectric constant was obtained from a frequency calculation using the PBE0+D2 functional (i.e., the one used for the geometry optimization). It is known[18] that the global hybrid functionals like PBE0 used here to calculate the vibrational contribution to the dielectric constant yields a lower value of ε_{vib} than GGA functionals like PBEsol, with the experimental values usually found between the values obtained using these two functionals.

In the present case, the results obtained with PBEsol seem in better agreement with the experiment; however, the dipolar contribution is still missing in the DFT estimation of the total dielectric constant. This contribution is supposed to be non-negligible in the perovskite material because the organic cation can move in the PbX_3 cage.[62] Unfortunately, the order of magnitude of this contribution is unknown and can only be computed using molecular or Monte-Carlo dynamics. Consequently, the apparently good results obtained by PBEsol can be a consequence of error cancellation reproducing the contribution of ε_{dip}. The overestimation of ε_{vib} by GGA functionals has been observed by some of us for several semiconductors.[18] The results obtained by hybrid functionals seem, for this property, in better agreement with the experiment, justifying the choice of the PBE0 functionals for these calculations.

Finally, assuming the sum of the electronic and vibrational contribution obtained in the present work is near the experimental one, the difference between the theoretical ε_r and the experimental one allows a tentative estimation of ε_{dip} that is around 10; so as large as the vibrational contribution. Nevertheless, although potentially high, the dipolar contribution is not taken into consideration in this article, since its absolute value is not computed and experimentally unknown.

Finally, the total dielectric constant of these materials, ε_r, ranges from 12.4 for $PbCl_3CH_3NH_3$ to 17.9 for $PbI_3CH_3NH_3$. This is half the value estimated by Brivio *et al.* with the PBEsol functional.[52]

These values target the requirement for the dielectric constant, preferably above a value of ~10, in agreement with the good efficiency measured for these compounds in photovoltaic devices.

2. The exciton binding energy.

In a perovskite solar cell, several paths can lead to the exciton dissociation: The transfer of the electron to TiO_2 (path (a)), the transfer of the hole to the spiro-OMeTAD (path (b)), the thermal dissociation leading to free carriers in the perovskite (path (c)) and the luminescence (path (d)). Each of these elementary processes is characterized by a specific time τ. All these steps are depicted in Figure 6 and listed in Table 5.

	Step	Time
(a)	$(e^- \leftrightarrow h^+) \rightarrow e^-_{TiO_2} + h^+_{PbX_3}$	< 1 ps[63]
(b)	$(e^- \leftrightarrow h^+) \rightarrow e^-_{PbX_3} + h^+_{spiro}$	0.66 ns[64]
(c)	$(e^- \leftrightarrow h^+) \rightarrow e^-_{PbX_3} + h^+_{PbX_3}$	
(d)	$(e^- \leftrightarrow h^+) \rightarrow h\upsilon$	4.5 ns[64]

Table 5. The four paths leading to the exciton dissociation.

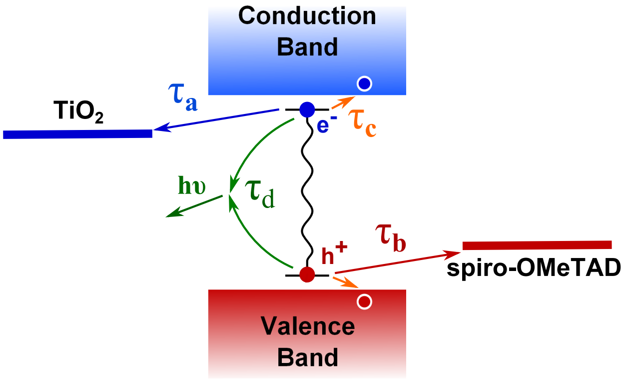

Figure 6. Scheme presenting the paths for exciton's dissociation with their characteristic times.

As explained in the paragraph dedicated to the dielectric constant, its vibrational contribution is associated to vibrational modes having frequencies around 100 cm^{-1}. For that reason, before ~300 fs (period of a 100 cm^{-1} frequency) the exciton is mainly subject to the electronic part of the dielectric constant ($\varepsilon = \varepsilon_\infty$) and after ~300 fs to both the electronic and the vibrational contributions ($\varepsilon = \varepsilon_\infty + \varepsilon_{vib} = \varepsilon_r$) leading to two values of the binding energies. These values are presented in the Figure 7. In that figure, the experimental values are not directly measured binding energies but values estimated using Wannier's model (equation (1)) with the experimental electronic part of the dielectric constant and the experimental effective masses.

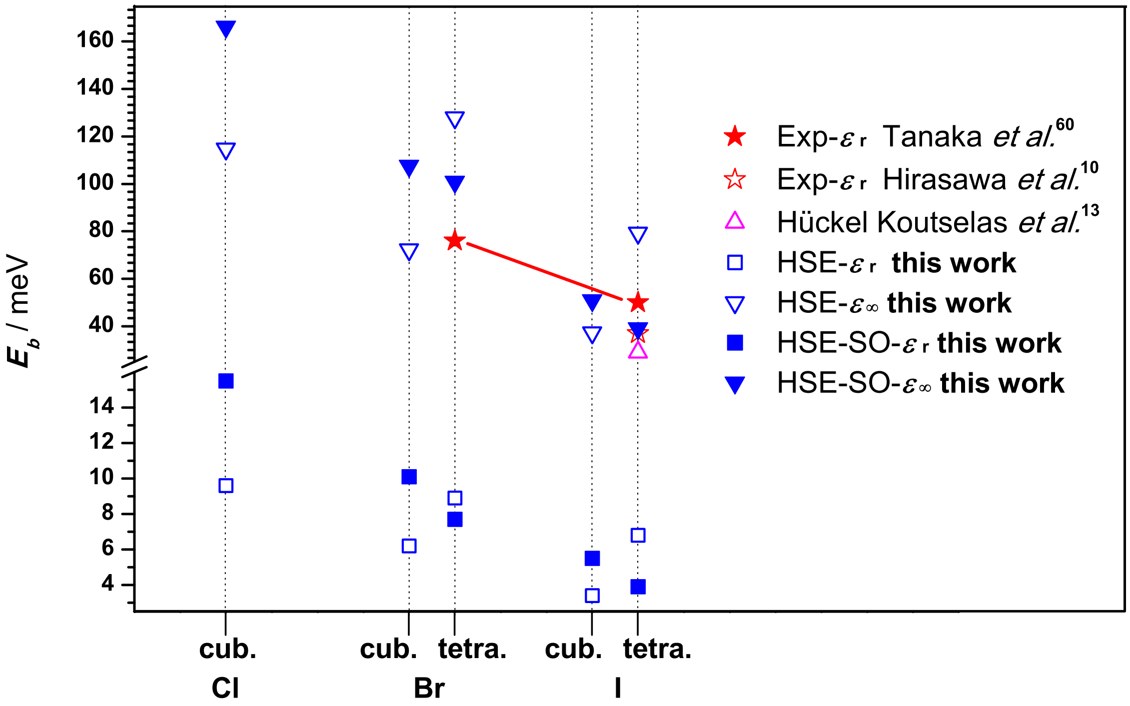

Figure 7. Computed and experimental exciton binding energies. The "-SO" label meaning "including spin-orbit coupling".

Interestingly, for all compounds, if only the electronic contribution is taken into account, $\boldsymbol{E_b}$ is higher than the thermal energy (~25 meV) showing that the exciton would be dissociated with difficulty at room temperature. If the vibrational contribution is added, the binding energies are reduced below 10 meV, leading to easily separable excitons. This confirms that vibrational contributions play an important role.

Thus, if τ_a and τ_b are higher than ~300 fs, photogenerated electrons and holes will be injected in TiO_2 and spiro-OMeTAD as free charge carriers while if τ_a and/or τ_b is lower than ~300 fs the injected charge will be bound in an exciton. These are two completely different working principle of solar cells since the first one (τ_a and $\tau_b > 300$ fs) corresponds to a standard thin film solar cell while the second one (τ_a and/or $\tau_b < 300$ fs) corresponds to an excitonic solar cell, like polymer based solar cells. In this last type of solar cell, exciton dissociation is the rate-determining step of the cell. In the case of Al_2O_3 sensitized solar cells, there is no electron transfer from the perovskite to the oxide. The electron diffuses toward the conductive glass inside the perovskite while Al_2O_3 only acts as a template agent. It can be reasonably assumed that the diffusion time of electrons from the perovskite to the conductive glass is higher than 1 ns, based on the work of Xing *et al.*[64] In that case, the dielectric constant felt by the exciton will be the static one, so the exciton will be dissociated before reaching the back contact, and the electron will be injected in the conductive oxide as free charge carrier and not bound in an exciton.

From the characteristic time known in that field (Table 5), for the TiO_2 sensitized perovskite cells, it is difficult to determine in which category of solar cell technology the perovskite based solar cells fall, since the injection time of the electron is unknown and probably near the separation criterion of 300 fs. Probably, some excitons are dissociated directly at the interfaces through electron injection into TiO_2 and some excitons are thermally dissociated (for instance the ones generated in the bulk perovskite, far from the interfaces) giving rise to free charge carriers within the perovskite. On the other hand, for Al_2O_3-sensitized perovskite cells, the behavior of the perovskite is more similar to that of an absorber in thin film technologies. The exciton is dissociated inside the perovskite and electrons and holes move as free charge carriers.

VI. Charge carrier diffusion: the effective masses

The effective masses of electrons and holes play an important role in semiconductors used in photovoltaic and photocatalytic devices since they are linked both to the exciton binding energy (Equation (1)) and to the mobilities of photogenerated free charge carriers as shown by equation (3) where $\boldsymbol{e}$ is the elementary charge, $\boldsymbol{\tau}$ the characteristic time for collisions and $\boldsymbol{m^*}$ the effective mass.

$$\mu = e\frac{\tau}{m^*} \tag{3}$$

The effective mass is a tensor property, its elements being associated to the different crystallographic directions. In the case of perovskite compounds, the effective masses were computed along the {100}, {110} and {111} directions for the cubic structures and along the {100}, {110}, {111}, {011} and {001} directions for the tetragonal structures. The harmonic average of the effective masses are depicted in the Figure 8 while the values computed in the different crystallographic directions are reported in Supporting Information. Spin-orbit coupling, although considerably increasing the computational requirements, was found to play a major role in the band curvature and hence in the effective masses.

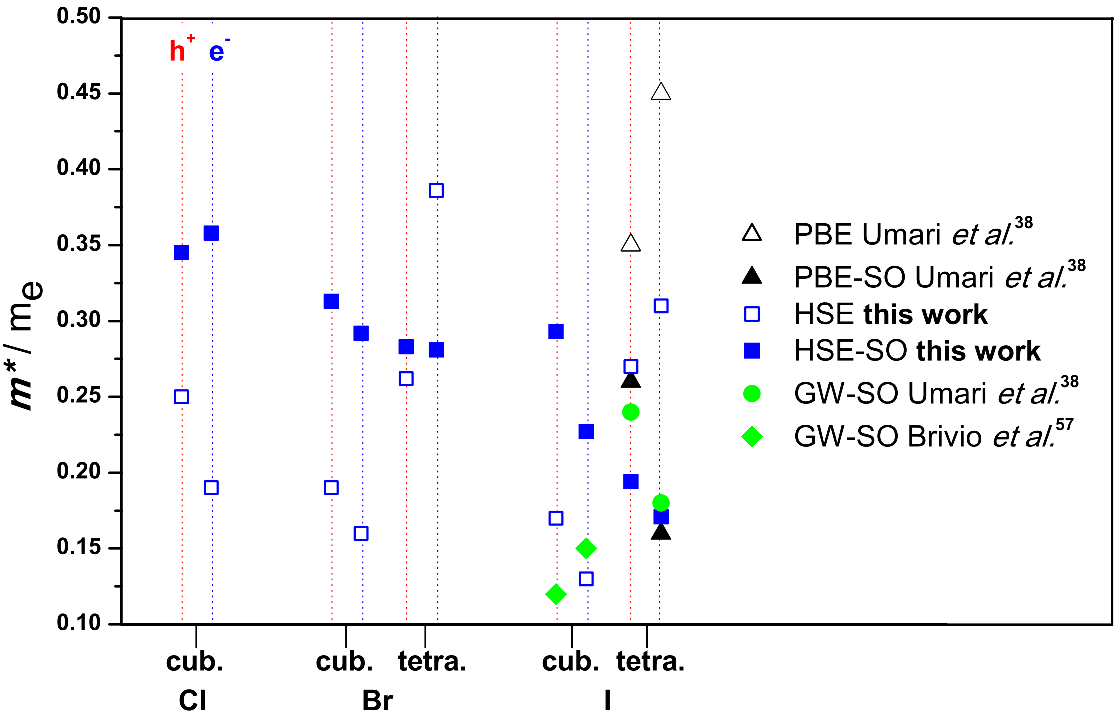

Figure 8. Harmonic average of the computed effective masses for holes and electrons. The "-SO" fragment meaning "including spin-orbit coupling".

One of the major influences of spin-orbit coupling on the electronic properties of the perovskite compounds is a modification of the band structure. Indeed, without spin-orbit coupling the bandgap of the cubic and the tetragonal phases are at the R-point and Γ-point of the Brillouin zone respectively. For the cubic $PbI_3CH_3NH_3$ and the tetragonal $PbI_3CH_3NH_3$ and $PbBr_3CH_3NH_3$ phases, this is no longer the case when the spin-orbit coupling is included in the Hamiltonian. In several directions, a slight offset of the bottom of the conduction band is observed, giving rise to an indirect bandgap as already mentioned in the section dedicated on the bandgap and as depicted in the example in Figure 9. This phenomenon has also been observed by Even *et al.*[65] and Kim *et al.*[66] for the cubic phase of $PbI_3CH_3NH_3$ and is shown here to be general for several phases of this family. In contrast, such an influence of spin-orbit coupling on the band structure is not observed for the $PbCl_3CH_3NH_3$ compound, suggesting that the halogen atom must be heavy enough to give rise to this phenomenon. It is interpreted by Kim *et al.* as an influence of the ferroelectric polarization on the Rashba bands.[66] Another consequence of spin-orbit coupling on the band structure is an increase in the curvature of the band in the directions for which the minimum of the conduction shifts from the symmetric ***k***-points. This leads to a noticeable reduction of the effective mass in these directions compared to the calculation without spin-orbit coupling (see Figure 9). Due to the strong influence of the spin-orbit coupling on the effective masses, these properties computed without the relativistic effect are meaningless and will not be discussed in this section. Moreover, as can be seen in Figure 9, the error made by computing the bandgap value using spin-orbit coupling at the Γ-point is below 5 meV when compared to the exact, indirect value of the bandgap. This error is negligible compared to the error of the used method, allowing to conclude that even when including spin-orbit-coupling the bandgap of these compounds is sufficiently well described through a computation at the Γ-point (for the tetragonal phases) and the R-point (for the cubic phases).

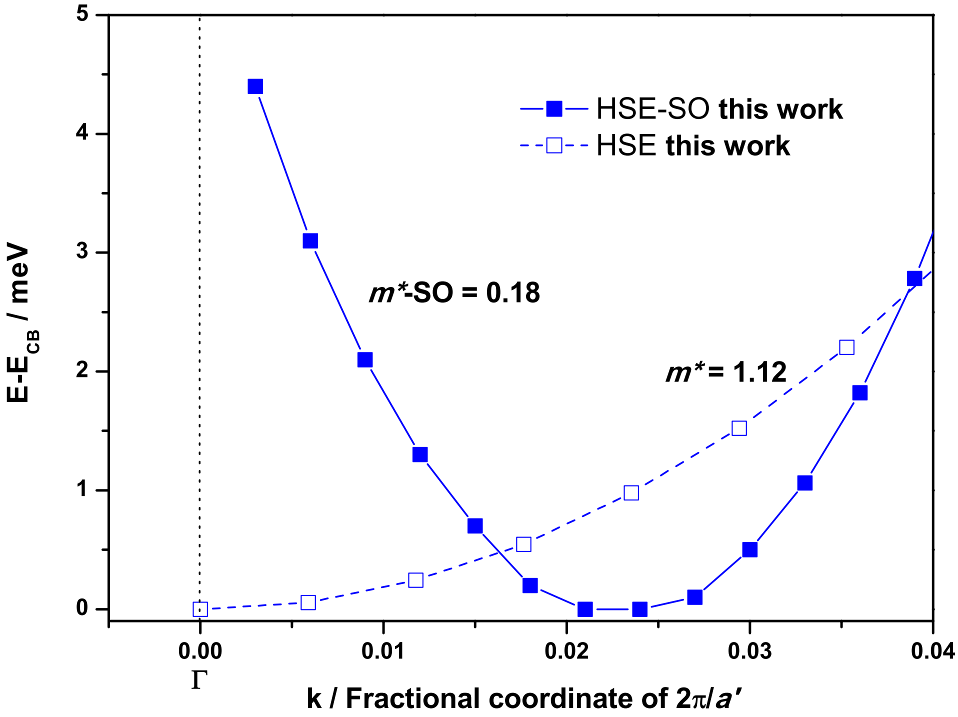

Figure 9. Dispersion curves of the conduction band of $PbI_3CH_3NH_3$ tetragonal phase in the {100} direction computed with HSE with and without the spin-orbit coupling. The effective masses extracted from the fitting these curves are also presented.

In the halogen series, the effective mass decreases with the increase of the halogen mass. This is probably a consequence of the higher covalency of the bonds involving heavy elements that have broader orbitals (p-orbitals in the case of halogens) favouring the overlap with the orbitals of the surroundings atom. This phenomenon was also observed in the chalcogen and picnogen series.[67,18]

For all compounds but $PbCl_3CH_3NH_3$ (for which holes and electrons have almost the same effective masses), the hole is slightly heavier than the electron, which is the expected behaviour since the hole is located on top of the valence band made of the p-orbitals of halogen ions, while the electron is in the conduction band composed of the more diffuse Pb 6p orbitals. The effective masses of the tetragonal phases are lower than the effective masses of the cubic phases.

Although the conductivity of the cubic phases should be lower than the conductivity of the tetragonal phases for the reasons explained above, the effective masses remain lower than 0.5 m_e, in agreement with the requirement set for this property (Table 1). For that reason all the $PbX_3CH_3NH_3$ compounds should be good electron and hole conductors, which is confirmed experimentally by the high hole mobility, 33 $cm^2.V^{-1}.s^{-1}$ established by Wehrenfenning *et al.*[68] for $PbI_{3-x}Cl_xCH_3NH_3$ and 66 $cm^2.V^{-1}.s^{-1}$ measured by Stoumpos *et al.*[69] for $PbI_3CH_3NH_3$.

Discussion and Conclusion

Recently, a steep increase in the number of publications on the $PbX_3CH_3NH_3$ family of perovskites (with X=I, Br, Cl) has appeared due to the discovery of their excellent photovoltaic properties. Several theoretical works based on quantum chemistry calculations on these materials were published in that field trying to understand the impressive photovoltaic properties of this family. These works comprise a range of computational methods ranging from the coarsest functionals in DFT to the most sophisticated post-DFT methods. While generally, the theoretical studies focused specifically on $PbI_3CH_3NH_3$, we decided to compute the properties of the five polymorphs that are stable above 200K – specifically the tetragonal and cubic phases for X=I, Br and the cubic phase for X=Cl – by using hybrid functionals which are known to be reliable functionals to compute semiconductor properties, in particular the range separated hybrid HSE. Comparing the results obtained in the present work to the ones published by other groups, several conclusions can be drawn:

1- Dispersion forces must be taken into account to accurately reproduce the geometries of these systems. The result of these forces can be artificially mimicked by using GGA functionals designed for solids (like PBEsol) or by using a small basis set for plane-wave basis set based codes.

2- Relativistic effects with spin-orbit coupling play a major role in the calculated band gaps, and strongly affect the band structure and hence the calculated effective masses. Agreement with experimental data in the absence of proper treatment of spin-orbit coupling is related to error cancelation.

3- The electron-hole interaction is strong as demonstrated by the failure of HSE to accurately reproduce the bandgap. Only very costly post-DFT calculations can correct for this error in a satisfactory manner.

4- The high dielectric constant of these materials is attributable both to relatively high vibrational contributions, as well as high polarization contributions. The latter term is better reproduced by DFT calculations than by post-DFT calculations. Furthermore, the vibrational term of the dielectric constant appeared to be relatively high. However, these calculations also put forward the high value of the dipolar contribution of the dielectric constant, which is as important as the vibrational term. The different characteristic times of the electronic and vibrational contributions of the dielectric constant leads to two exciton binding energies depending on whether the exciton is dissociated at the interface before ~300 fs or not. This shows the possibility of having several interfacial charge transfer mechanisms in these perovskite materials.

5- The diffuse character of valence orbitals on the heavy elements (Pb or halogen) give rise to a high polarizability and low effective charge carrier masses. In turn, these effects yield low values for the exciton binding energies. Element substitution (of Pb for example) would require the use of other relatively heavy elements.

6- The perovskite materials show a high charge carrier mobility and hence an intrinsic carrier transport function. This explains the efficiency of devices using an Al_2O_3 support instead of a TiO_2 support, where the carrier transport has to be performed by the perovskite itself.

In Table 6, the value obtained by using the state of the art method for each property has been provided.

$PbCl_3CH_3NH_3$ (cubic)

Property	E_g / eV	ε_∞	ε_r	E_b / meV	$\bar{m}_e^*$ / m_e	$\bar{m}_h^*$ / m_e
Method	HSE	HSE-SO	HSE-SO	HSE-SO	HSE-SO	HSE-SO
Value	2.81	3.8	12.4	15.5	0.36	0.34

$PbBr_3CH_3NH_3$ (cubic)

Property	E_g / eV	ε_∞	ε_r	E_b / meV	$\bar{m}_e^*$ / m_e	$\bar{m}_h^*$ / m_e
Method	HSE	HSE-SO	HSE-SO	HSE-SO	HSE-SO	HSE-SO
Value	2.31	4.4	14.2	10.1	0.29	0.31

$PbBr_3CH_3NH_3$ (tetragonal)

Property	E_g / eV	ε_∞	ε_r	E_b / meV	$\bar{m}_e^*$ / m_e	$\bar{m}_h^*$ / m_e
Method	HSE	HSE-SO	HSE-SO	HSE-SO	HSE-SO	HSE-SO
Value	2.56	4.4	15.7	7.7	0.28	0.28

$PbI_3CH_3NH_3$ (cubic)

Property	E_g / eV	ε_∞	ε_r	E_b / meV	$\bar{m}_e^*$ / m_e	$\bar{m}_h^*$ / m_e
Method	GW-SO[57]	HSE-SO	HSE-SO	HSE-SO	HSE-SO	HSE-SO
Value	1.67	5.8	17.8	5.5	0.13	0.17

$PbI_3CH_3NH_3$ (tetragonal)

Property	E_g / eV	ε_∞	ε_r	E_b / meV	$\bar{m}_e^*$ / m_e	$\bar{m}_h^*$ / m_e
Method	GW-SO[38]	GW-SO[38]	HSE-SO	HSE-SO	GW-SO[38]	GW-SO[38]
Value	1.67	7.1	17.7	3.9	0.18	0.24

Table 6. Electronic properties computed for all the compounds investigated in this publication. The values were selected based on a compromise between the global accuracy of the method and the agreement with the experimental value (when available). The "-SO" fragment meaning "including spin-orbit coupling".

Concluding, this family of compounds presents a number of challenges to the theoretical chemist such as simultaneously accounting for dispersion forces, relativistic effects, electron-hole interaction and the dynamics of the organic cation leading to a strong polarization contribution in the dielectric constant. Some of these difficulties can be overcome using very sophisticated methods (like GW calculations), but at computational costs prohibitive for their use in the modelling of large systems (such as interfaces). Some groups[51] suggested to adapt the functionals to the system, using the method proposed by Marques *et al.*[70,71] Although effective, this method relies on non-transferable functionals and makes it difficult to adapt the functional if several materials are in contact (like in the modelling of the $TiO_2/PbX_3CH_3NH_3$ interface). A pragmatic solution would be to use the PBEsol functional, since it reproduces several properties at low computational cost (but thanks to error cancelations). The calculations presented here can already provide very useful semi-quantitative insights in order to understand their properties and compare different species in the same family. In this way they can potentially serve to design even more performing materials.

Acknowledgement.

We wish to thank Ilaria Ciofini (Chimie Paristech) for helpful comments and discussions. We acknowledge the IDRIS and PSMN calculation centers for providing computational resources.

Supporting Information.

The numeric values computed for this study and obtained from the literature for all the properties are presented in supporting information. The IR spectra used to compute the vibrational contribution to the dielectric constant are also presented. All the geometries optimized at the PBE0+D2 level are also in supporting information.

References

1. A. Hagfeldt, G. Boschloo, L. Sun, L. Kloo, and H. Pettersson, *Chem. Rev.*, 2010, **110**, 6595–6663.

2. A. Kojima, K. Teshima, Y. Shirai, and T. Miyasaka, *J. Am. Chem. Soc.*, 2009, **131**, 6050–6051.

3. M. M. Lee, J. Teuscher, T. Miyasaka, T. N. Murakami, and H. J. Snaith, *Science*, 2012, **338**, 643–647.

4. J.-H. Im, C.-R. Lee, J.-W. Lee, S.-W. Park, and N.-G. Park, *Nanoscale*, 2011, **3**, 4088–4093.

5. J. H. Noh, S. H. Im, J. H. Heo, T. N. Mandal, and S. Il Seok, *Nano Lett.*, 2013, **13**, 1764–1769.

6. B. Cai, Y. Xing, Z. Yang, W.-H. Zhang, and J. Qiu, *Energ. Environ. Sci.*, 2013, **6**, 1480–1485.

7. S. Kazim, M. K. Nazeeruddin, M. Grätzel, and S. Ahmad, *Angew. Chem. Int. Ed.*, 2014, **53**, 2812–2824.

8. M. A. Green, K. Emery, Y. Hishikawa, W. Warta, and E. D. Dunlop, *Prog. Photovolt Res. Appl.*, 2014, **22**, 701–710.

9. D. Weber, *Z. Naturforsch B*, 1978, **33**, 1443–1445.

10. M. Hirasawa, T. Ishihara, T. Goto, K. Uchida, and N. Miura, *Phys. B*, 1994, **201**, 427–430.

11. T. Ishiharat, *J. Lumin.*, 1994, **61**, 269–274.

12. G. C. Papavassiliou and I. B. Koutselas, *Synth. Met.*, 1995, **71**, 1713–1714.

13. I. B. Koutselas, L. Ducasse, and G. C. Papavassiliou, *J. Phys. Condens. Matter*, 1996, **8**, 1217–1227.

14. H. Mashiyama and Y. Kurihara, *J. Korean Phys. Soc.*, 1998, **32**, 156–158.

15. I. P. Swainson, R. P. Hammond, C. Soullière, O. Knop, and W. Massa, *J. Solid State Chem.*, 2003, **176**, 97–104.

16. L. Chi, I. Swainson, L. Cranswick, J.-H. Her, P. Stephens, and O. Knop, *J. Solid State Chem.*, 2005, **178**, 1376–1385.

17. A. Poglitsch and D. Weber, *J. Chem. Phys.*, 1987, **87**, 6373–6378.

18. T. Le Bahers, M. Rérat, and P. Sautet, *J. Phys. Chem. C*, 2014, **118**, 5997–6008.

19. C. R. Dovesi, V. R. Saunders, Roetti, R. Orlando, C. M. Zicovich-Wilson, F. Pascale, B. Civalleri, K. Doll, N. M. Harrison, I. J. Bush, P. D'Arco, M. Llunell, M. Causà, and Y. Noël, 2014, CRYSTAL14 User's Manual (University of Torino)

20. R. Dovesi, R. Orlando, A. Erba, C. M. Zicovich-Wilson, B. Civalleri, S. Casassa, L. Maschio, M. Ferrabone, M. De La Pierre, P. D'Arco, Y. Noël, M. Causà, M. Rérat, and B. Kirtman, *Int. J. Quantum Chem.*, 2014, **114**, 1287–1317.

21. J. Perdew, K. Burke, and M. Ernzerhof, *Phys. Rev. Lett.*, 1996, **77**, 3865–3868.

22. J. Perdew, A. Ruzsinszky, G. Csonka, O. Vydrov, G. Scuseria, L. Constantin, X. Zhou, and K. Burke, *Phys. Rev. Lett.*, 2008, **100**, 136406.

23. C. Adamo and V. Barone, *J. Chem. Phys.*, 1999, **110**, 6158–6170.

24. A. D. Becke, *J. Chem. Phys.*, 1993, **98**, 5648–5652.

25. P. C. Hariharan and J. A. Pople, *Theor. Chim. Acta*, 1973, **28**, 213–222.

26. M. F. Peintinger, D. V. Oliveira, and T. Bredow, *J. Comput. Chem.*, 2013, **34**, 451–459.

27. R. Weihrich and I. Anusca, *Z. Anorg. Allg. Chem.*, 2006, **632**, 335–342.

28. S. Grimme, *J. Comput. Chem.*, 2004, **25**, 1463–73.

29. Y. Noel, C. Zicovich-Wilson, B. Civalleri, P. D'Arco, and R. Dovesi, *Phys. Rev. B*, 2001, **65**, 014111.

30. J. Heyd, G. E. Scuseria, and M. Ernzerhof, *J. Chem. Phys.*, 2006, **124**, 219906.

31. J. Heyd, G. E. Scuseria, and M. Ernzerhof, *J. Chem. Phys.*, 2003, **118**, 8207–8215.

32. G. Kresse and J. Furthmiiller, *Comput. Mater. Sci.*, 1996, **6**, 15–50.

33. G. Kresse and J. Furthmüller, *Phys. Rev. B*, 1996, **54**, 11169–11186.

34. R. Hafner, *J. Comput. Chem.*, 2008, **28**, 2044–2078.

35. G. Kresse and D. Joubert, *Phys. Rev. B*, 1999, **59**, 11–19.

36. D. Hobbs, G. Kresse, and J. Hafner, *Phys. Rev. B*, 2000, **62**, 11556–11570.

37. S. Colella, E. Mosconi, P. Fedeli, A. Listorti, F. Gazza, F. Orlandi, P. Ferro, T. Besagni, A. Rizzo, G. Calestani, G. Gigli, F. De Angelis, and R. Mosca, *Chem. Mater.*, 2013, **25**, 4613–4618.

38. P. Umari, E. Mosconi, and F. De Angelis, *Sci. Rep.*, 2014, **4**, 4467.

39. E. Mosconi, A. Amat, K. Nazeeruddin, M. Gra, and F. De Angelis, *J. Phys. Chem. C*, 2013, **117**, 13902–13913.

40. P. Giannozzi, S. Baroni, N. Bonini, M. Calandra, R. Car, C. Cavazzoni, D. Ceresoli, G. L. Chiarotti, M. Cococcioni, I. Dabo, A. Dal Corso, S. de Gironcoli, S. Fabris, G. Fratesi, R. Gebauer, U. Gerstmann, C. Gougoussis, A. Kokalj, M. Lazzeri, L. Martin-Samos, N. Marzari, F. Mauri, R. Mazzarello, S. Paolini, A. Pasquarello, L. Paulatto, C. Sbraccia, S. Scandolo, G. Sclauzero, A. P. Seitsonen, A. Smogunov, P. Umari, and R. M. Wentzcovitch, *J. Phys. Condens. Matter*, 2009, **21**, 395502.

41. G. Giorgi, J. Fujisawa, H. Segawa, and K. Yamashita, *J. Phys. Chem. Lett.*, 2013, **4**, 4213–4216.

42. J. Heyd and G. E. Scuseria, *J. Chem. Phys.*, 2004, **121**, 1187–1192.

43. J. Klimeš, D. R. Bowler, and A. Michaelides, *Phys. Rev. B*, 2011, **83**, 195131.

44. F. Labat, I. Ciofini, and C. Adamo, *J. Chem. Phys.*, 2009, **131**, 044708.

45. J. Paier, M. Marsman, K. Hummer, G. Kresse, I. C. Gerber, and J. G. Angyán, *J. Chem. Phys.*, 2006, **124**, 154709.

46. F. Labat, P. Baranek, C. Domain, C. Minot, and C. Adamo, *J. Chem. Phys.*, 2007, **126**, 154703.

47. A. Dal Corso, *Pb.pbe-dn-rrkjus_psl.0.2.2.UPF*, 2012.

48. P. Pulay, *Mol. Phys.*, 1969, **17**, 197–204.

49. D. a. Egger and L. Kronik, *J. Phys. Chem. Lett.*, 2014, **5**, 2728–2733.

50. Y. Wang, T. Gould, J. F. Dobson, H. Zhang, H. Yang, X. Yao, and H. Zhao, *Phys. Chem. Chem. Phys.*, 2014, **16**, 1424–1429.

51. E. Menéndez-Proupin, P. Palacios, P. Wahnón, and J. C. Conesa, *Phys. Rev. B*, 2014, **90**, 045207.

52. F. Brivio, A. B. Walker, and A. Walsh, *APL Mat.*, 2013, **1**, 042111.

53. W. Shockley and H. J. Queisser, *J. Appl. Phys.*, 1961, **32**, 510–519.

54. R. R. Lunt, T. P. Osedach, P. R. Brown, J. a. Rowehl, and V. Bulović, *Adv. Mat.*, 2011, **23**, 5712–5727.

55. G. C. Papavassiliou, G. A. Mousdis, and G. C. Anyfantis, *Z. Naturforsch B*, 2010, **65**, 516–520.

56. J. Even, L. Pedesseau, J.-M. Jancu, and C. Katan, *J. Phys. Chem. Lett.*, 2013, **4**, 2999–3005.

57. F. Brivio, K. T. Butler, A. Walsh, and M. van Schilfgaarde, *Phys. Rev. B*, 2014, **89**, 155204.

58. J. Even, L. Pedesseau, J.-M. Jancu, and C. Katan, *Phys. Status Solidi PRL*, 2014, **8**, 31–35.

59. G. Onida, I. Nazionale, R. T. Vergata, R. Scientifica, and I.- Roma, *Rev. Mod. Phys.*, 2002, **74**, 601–659.

60. K. Tanaka, T. Takahashi, T. Ban, T. Kondo, K. Uchida, and N. Miura, *Solid State Comm.*, 2003, **127**, 619–623.

61. G. Lucovsky, R. M. White, W. Y. Liang, R. Zallen, and P. Schmid, *Solid State Comm.*, 1976, **18**, 811–814.

62. M. A. Green, A. Ho-Baillie, and H. Snaith, *Nat. Photonics*, 2014, **8**, 506–514.

63. C. S. Ponseca, T. J. Savenije, M. Abdellah, K. Zheng, A. Yartsev, T. Pascher, T. Harlang, P. Chabera, T. Pullerits, A. Stepanov, J.-P. Wolf, and V. Sundström, *J. Am. Chem. Soc.*, 2014, **136**, 5189–5192.

64. G. Xing, N. Mathews, S. Sun, S. S. Lim, Y. M. Lam, M. Grätzel, S. Mhaisalkar, and T. C. Sum, *Science*, 2013, **342**, 344–347.

65. J. Even, L. Pedesseau, and C. Katan, *J. Phys. Chem. C*, 2014, **118**, 11566–11572.

66. M. Kim, J. Im, A. J. Freeman, J. Ihm, and H. Jin, *PNAS*, 2014, **111**, 6900–6904.

67. I. Vurgaftman, J. R. Meyer, and L. R. Ram-Mohan, *J. Appl. Phys.*, 2001, **89**, 5815–5875.

68. C. Wehrenfennig, M. Liu, H. J. Snaith, M. B. Johnston, and L. M. Herz, *Energ. Environ. Sci.*, 2014, **7**, 2269–2275.

69. C. C. Stoumpos, C. D. Malliakas, and M. G. Kanatzidis, *Inorg. Chem.*, 2013, **52**, 9019–9038.

70. M. A. L. Marques, J. Vidal, M. J. T. Oliveira, L. Reining, and S. Botti, *Phys. Rev. B*, 2011, **83**, 035119.

71. J. C. Conesa, *Catal. Today*, 2013, **208**, 11–18.